Appl. Phys. B (2014) 116:681–698
DOI 10.1007/s00340-013-5752-3

Applied Physics B
Lasers and Optics

Improvements in filtered Rayleigh scattering measurements using Fabry–Perot etalons for spectral filtering of pulsed, 532-nm Nd:YAG output

Jeffrey A. Sutton · Randy A. Patton

Received: 14 September 2013 / Accepted: 16 December 2013 / Published online: 1 January 2014

Abstract In this manuscript, we investigate a new methodology for increasing the spectral purity of the second-harmonic output of an injection-seeded, frequency-doubled, Q-switched Nd:YAG laser operating near 532 nm. Specifically, tunable Fabry–Perot etalons (FPEs) are used as ultra-narrowband spectral filters, transmitting the desired single-mode output, while filtering out a significant portion of the broadband pedestal characteristic of injection-seeded lasers. A specific emphasis is placed on the design and optimization of the FPEs in the context of filtered Rayleigh scattering (FRS) measurements and how their utilization results in substantial increases in spectral purity, realizable attenuation of unwanted scattering, and applications in environments with high particulate levels. Experimental results show an increase in laser spectral purity of more than one order-of-magnitude (from 0.99997 to 0.999998) when using FPE filters, which led to a two-order-of-magnitude increase in achievable attenuation of laser light passing through a molecular iodine filter. The utility of the FPE-based spectral filtering of the pulsed Nd:YAG output for 2D FRS imaging was demonstrated in turbulent, isothermal gas-phase jets, seeded with varying levels of non-evaporating droplets with particle volume fractions (F_{Vp}) ranging from $\sim$5 to >60 parts-per-million (ppm). After implementation of an optimized air-spaced FPE in the 532-nm output, no particle scattering was observed (based on visual and statistical analysis), even for the highest seed case ($F_{Vp} \sim 60$ ppm), and the gas-phase Rayleigh–Brillouin signals were collected without interference from the flowfield particulate. The current results suggest that the implementation of properly specified FPEs allows FRS to be applied in environments with high flowfield particulate levels; levels are well beyond what have been suitable for previous FRS measurements.

J. A. Sutton (✉) · R. A. Patton
Department of Mechanical and Aerospace Engineering, Ohio State University, Columbus, OH, USA
e-mail: sutton.235@osu.edu

1 Introduction

Laser Rayleigh scattering (LRS) is a well-known measurement technique which can be used to provide gas-phase density, temperature, and bulk velocity data. However, in many circumstances, flowfield particle scattering and/or stray light from surface (i.e., wall or window) scattering can overwhelm gas-phase information of interest. Filtered Rayleigh scattering (FRS) is a variant of traditional LRS in which a narrow-linewidth laser illuminates a sample volume, and the scattered light is collected by a detector outfitted with an atomic or molecular filter to discriminate gas-phase scattering from unwanted background scattering (i.e., particles or surfaces) [e.g., 1–6]. Previously, FRS has been used for flow visualization and density and velocity measurements in high-speed confined flows [e.g., 1, 2, 4, 6–8] as well as temperature measurements in environments with high levels of surface scattering [9, 10] or flowfield particulate such as sooting flames [e.g., 11, 12] and seeded flows for particle imaging velocimetry (PIV) measurements [e.g., 10, 13, 14]. Strong rejection of the interfering particle or surface scattering is accomplished by spectrally tuning the laser output to coincide with an absorption transition of the gas used within the atomic/molecular filter cell. Background scattering from surfaces ("stray light") has the same frequency distribution as the laser and particle scattering exhibits essentially the same frequency distribution as the laser with a spectral shift which is a function of velocity. For a

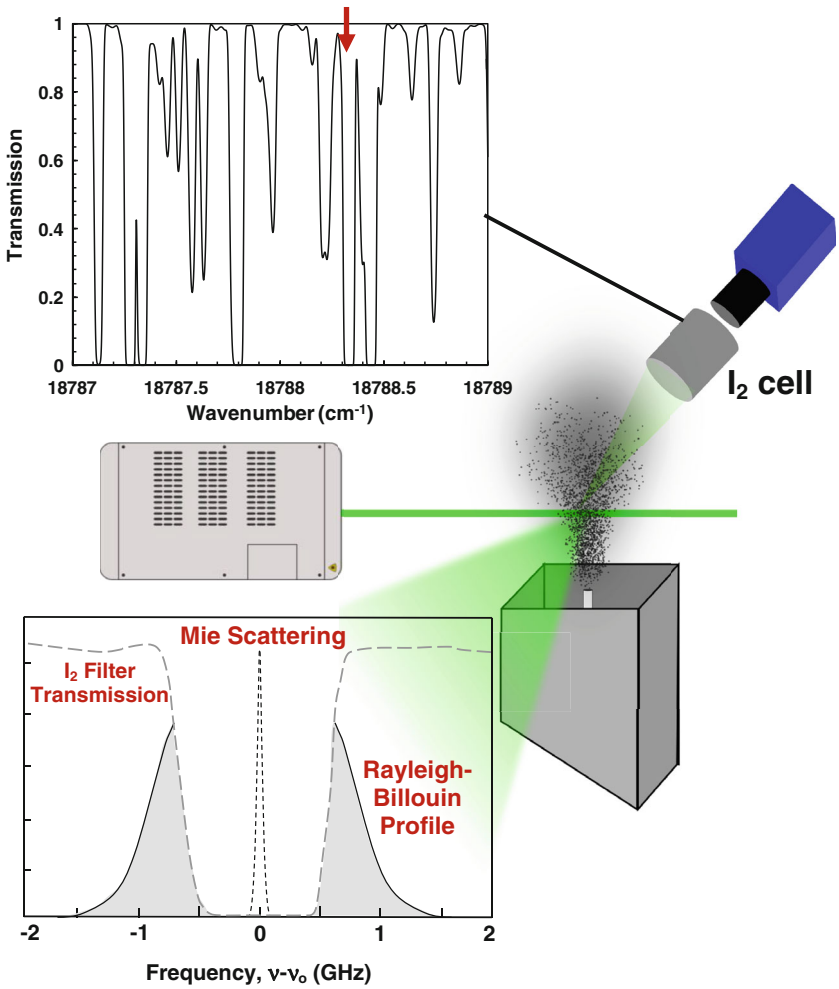

Fig. 1 Filtered Rayleigh scattering (FRS) concept depicting the use of a combination of an Nd:YAG laser and molecular iodine (I_2) filter. Shown at the top is a modeled I_2 absorption spectra in the vicinity of Nd:YAG laser output. The feature marked with an *arrow* was used for the results shown in Fig. 11–15. The outset in the bottom depicts the overlap of the I_2 filter transmission profile with unwanted particle/surface scattering and the Rayleigh–Brillouin scattering from gas-phase molecules

spectrally-narrow laser source with a linewidth (ν_L) narrower than the absorption transition of the atomic/molecular filter species, the laser lineshape and the unwanted light scattering from surfaces and/or particulate can be absorbed effectively by the filter cell. Scattering from gas-phase species is broadened by a combination of thermal and acoustic motion and is described by a Rayleigh–Brillouin lineshape, which is quite broad in comparison with the narrow laser lineshape. As shown in the graphical representation of the technique depicted in Fig. 1, a portion of the Rayleigh–Brillouin scattering spectrum falls outside of the filter absorption band and is transmitted to the detector.

Previously, the majority of FRS studies have been performed in the visible regime using the combination of a frequency-doubled, Nd:YAG laser at 532 nm and a molecular iodine (I_2) filter [e.g., 1–19]. Additional studies in the ultraviolet regime have been presented by combining the frequency-tripled output of an alexandrite or titanium/sapphire laser at 254 nm with an atomic mercury filter [e.g., 20–23]. However, operating in the visible regime continues to offer the advantages of commercially-available, high-energy, frequency-doubled, injection-seeded, Q-switched, Nd:YAG lasers and low-noise, highly sensitive CCD cameras.

A common limitation reported with visible FRS measurements is the decreased rejection of the unwanted light scattering as compared to theoretical model results when using Q-switched, injection-seeded, frequency-doubled Nd:YAG lasers [e.g., 3, 12, 15, 19]. Examples include the initial work of Forkey [3] who developed a comprehensive model to describe the absorption spectrum of iodine vapor as a function of filter parameters. In his Ph.D. dissertation work, model calculations predicted a minimum transmission near 18,788.44 cm^{-1} of $<10^{-6}$ for a cell length of 243 mm, cell temperature of 353 K, and I_2 vapor pressure of 0.46 Torr. Measurements acquired with a single-frequency ($\nu_L \sim 5$ kHz) continuous wavelength (CW) Nd:YAG laser experimentally confirmed the theoretical absorption strengths to within 10 %. However, the measured minimum transmission was significantly higher at $\sim 10^{-3}$ when using an injection-seeded, frequency-doubled,

Q-switched, Nd:YAG laser. Measurements reported by Seasholtz and Buggele [15] and Kearney et al. [12] demonstrated similar results; that is, measured attenuation was significantly lower than that expected from modeling results. In particular, for the experimental conditions of Seasholtz and Buggele [15], the iodine absorption model predicts a minimum transmission of 5×10^{-6} near 18,788.44 cm^{-1} for a 200-mm-long cell at 323 K containing 0.46 Torr of I_2 vapor. The measured minimum transmission reported by Seasholtz and Buggele [15] was 3×10^{-3}. In the work of Kearney et al. [12], the frequency-doubled output of the Nd:YAG laser was tuned to the R121 (35-0) transition near 18,789.25 cm^{-1}. The I_2 filter cell was 254 mm, operating at 353 K with an I_2 vapor pressure of 1.5 Torr. Based on theoretical models [3, 17, 24], the minimum transmission is calculated as $<10^{-8}$; however, experimental measurements yielded a minimum transmission of only 10^{-3}, consistent with the aforementioned work. Finally, in our recent work [19], we tuned our pulsed laser to the R56(32,0) transition near 18,788.33 cm^{-1} and operated our 254-mm-long I_2 cell at 341 K and a cell pressure of 1.05 Torr. For these conditions, the theoretical model of Forkey [3, 17] predicts a minimum transmission of $\sim 5 \times 10^{-9}$; however, our experimental results showed a minimum transmission between 10^{-4} and 10^{-5}, depending on laser seed power (and the resultant spectral purity of the laser). While these are the highest extinction ratios reported within the literature, they are still several orders of magnitude below theoretical predictions.

As we discussed in previous work [19], an accepted consensus for the limited scattering rejection is that the output of an injection-seeded, Q-switched Nd:YAG is likely a spectrally-narrow peak (i.e., single longitudinal mode) superimposed onto a pedestal of additional weak longitudinal modes ("broadband pedestal") due to residual mode competition within the oscillator [3, 12, 15]; a fact that is somewhat inherent to the injection-seeding process. As discussed in Refs. [12] and [19], the implications of a weak "broadband pedestal" for FRS measurements are very important since a number of these additional longitudinal modes forming the low-energy pedestal may fall outside of the I_2 absorption feature. Since particle and background scattering is much more intense than gas-phase Rayleigh–Brillouin scattering, even the residual laser energy in the pedestal can lead to significant interference and a reduction in the effectiveness of the I_2 molecular filter. As we demonstrated previously [19], the realizable attenuation of unwanted scattering is severely limited by the spectral purity of the laser, which decreases as the small, broadband, non-seeded component of the laser increases. Results from a set of calculations showed a logarithmic relationship between laser spectral purity and the effective optical density of the I_2 filter; that is, for every order of magnitude decrease in spectral purity, there was a corresponding order of magnitude decrease in achievable optical density. As one example, for a 254-mm-long I_2 cell operating at 341 K and a cell pressure of 1.05 Torr, a decrease in spectral purity from 1 to 0.999999 and 1 to 0.999 results in an estimated increase in the minimum transmission from $\sim 5 \times 10^{-9}$ to $\sim 10^{-6}$ and $\sim 10^{-3}$, respectively.

In this manuscript, we investigate a new method for increasing the effective spectral purity of the pulsed 532-nm output by filtering out a significant portion of the broadband pedestal with tunable Fabry–Perot etalons (FPEs) placed within the optical beam path. A specific emphasis is placed on the design and optical properties of the FPEs in the context of FRS imaging and how this translates into substantial increases in spectral purity and an increase in attenuation of unwanted scattering by more than two orders of magnitude. We show that the implementation of properly specified FPEs allows FRS to be applied in environments with high flowfield particulate levels; levels are well beyond what have been suitable for previous FRS measurements.

2 Experimental setup

A complete schematic of the experimental setups used for the current work is shown in Fig. 2. Two experimental configurations are used: (a) a *transmission scan configuration* as shown in Fig. 2a and (b) a *FRS imaging configuration* as shown in Fig. 2b. At the core of both configurations is an injection-seeded, frequency-doubled, Q-switched, Nd:YAG laser (Spectra-Physics Pro 290; 1) operating at a repetition rate of 10 Hz with output energies up to 750 mJ/pulse. Starting with the *transmission scan configuration*, the 532-nm output passes through a combination of a half-waveplate (2) and thin-film polarizer (3) for variable pulse energy attenuation. The beam then passes through an iris (4) such at the central 80 % of the beam is used for the scanning measurements. In this study, the iris is used as a precautionary measure to minimize spatial variations in the optical frequency of the injection-seeded (unstable-resonator) Q-switched Nd:YAG laser output [16]. By eliminating the outermost portion of the beam, it is estimated that any frequency variations across the beam can be reduced to tens of MHz. After passing through the iris, the beam transmits through a tunable Fabry–Perot etalon (FPE; 5) mounted on a two-axis rotation stage. The FPE is used as a spectral filter for the pulsed, 532-nm beam and will be described in detail below. After passing through the FPE, the 532-nm beam is reflected off of two mirrors (6), passes through an additional iris, a 60/40 beamsplitter

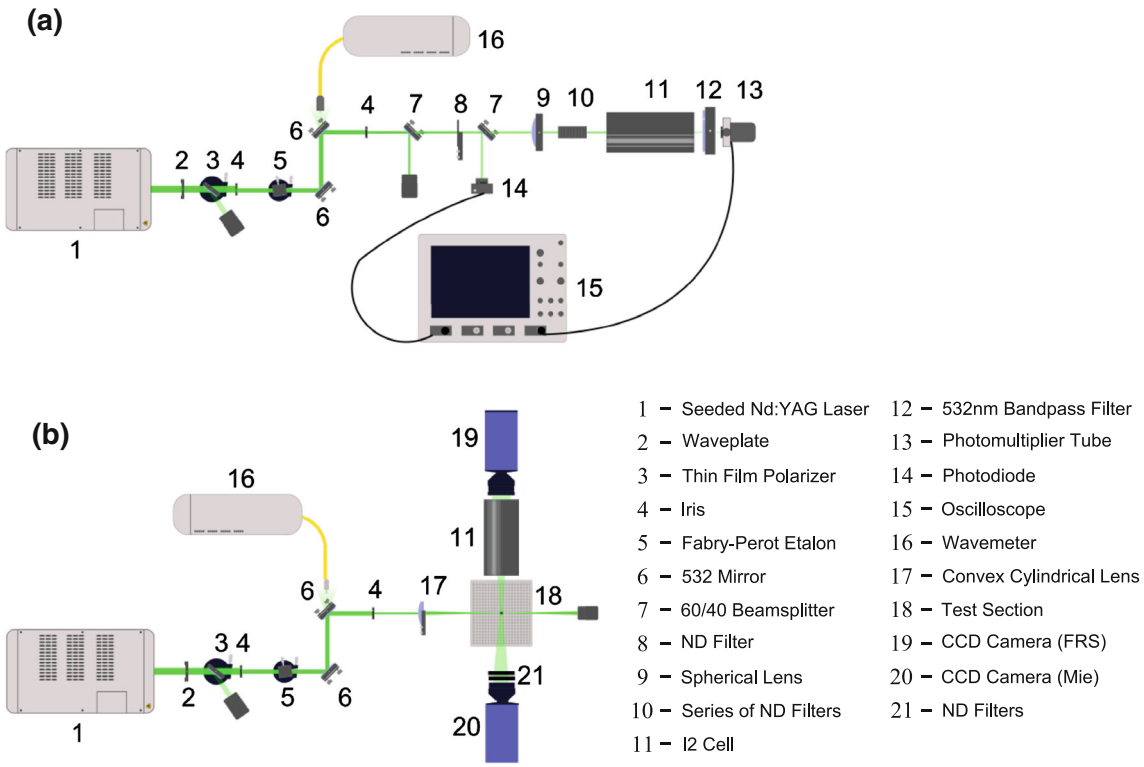

Fig. 2 Schematic of the two experimental configurations used in the present study. **a** transmission scan configuration **b** FRS imaging configuration

(7), a neutral density (ND) filter, and a second 60/40 beamsplitter. Due to finite reflectivity of the mirrors (~99.9 %), a small portion of the laser beam passes through the second mirror and is collected by a single-mode optical fiber and is passed to a high-resolution wavemeter (High Finesse, WS-U, 16) with an absolute accuracy of 30 MHz in frequency position and a spectral linewidth measurement resolution of 75 MHz. The wavemeter is automatically calibrated twice per hour by an additional fiber-optically-coupled, frequency-stabilized, Helium–Neon laser operating near 632 nm.

The portion of the beam that is reflected via the second 60/40 beamsplitter is sent to a photodiode (PD; Thorlabs DET10A; rise time <1 ns; 14) for pulse-to-pulse laser energy monitoring. The portion of the beam transmitted through the second 60/40 beamsplitter is focused through a plano-convex spherical lens (9), a series of fixed and removable, user-calibrated ND filters (10), the temperature-controlled, molecular iodine cell (11), a 532-nm bandpass filter (12), and onto a photomultiplier tube (PMT, Hamamatsu PR1405CE; 13). The 532-nm bandpass filter is placed between the I_2 cell and the PMT to block I_2 laser-induced fluorescence. The maximum 532-nm pulse energy that passes through the I_2 cell is <10 μJ/pulse, which corresponds to an estimated peak laser intensity of $<6 \times 10^2$ W/cm^2. This is more than four orders of magnitude less than the estimated saturated intensity of I_2 ($\sim 10^7$ W/cm^2) at the cell conditions; thus, saturation effects are avoided. The outputs from the PD and PMT are recorded on a digital oscilloscope (LeCroy Waverunner 104MXi; 15) with an analog bandwidth of 1 GHz and a sampling resolution of 100 ps.

The 254-mm-long, 76-mm-diameter I_2 filter cell (Innovative Scientific Solutions, Inc.) is a starved-cell configuration based on the design described in [8]. The cell was filled with a sidearm temperature of 313 K (1.05 Torr I_2) and closed off, thus fixing the I_2 number density within the cell. The main body of the cell is surrounded by electrical resistance heating tape and operated at a super-heated temperature of 341 K to ensure no vapor recrystallizes to the solid phase within the filter cell. The cell is maintained at the specified temperature by a digital temperature controller (Cole-Parmer DigiSense) which has a quoted accuracy of 0.1 K.

Subsequently, for the *FRS imaging configuration*, the 532-nm output first passes through a combination of a half-waveplate (2) and thin-film polarizer (3) for variable pulse energy attenuation. The beam then passes through an iris (4) such that only the central 80 % of the beam is used for the imaging as in the scanning measurements. After passing through the first iris, the beam transmits through a tunable Fabry–Perot etalon (FPE; 5) mounted on a two-axis

rotation stage and is reflected off two 532-nm mirrors (6), where a small portion of 532-nm light that leaks through the mirror substrate is collected via fiber optic and sent to the high-resolution wavemeter (16) for pulse-to-pulse frequency monitoring. After passing through a second iris (matched in size to the first iris), the 532-nm beam is formed into a 10×0.17 mm^2 laser sheet by a single $f = 500$ mm, plano-convex cylindrical lens (17) and passed through the measurement test section (18). The laser sheet thickness is reported as the $1/e^2$ value and was determined by rotating the cylindrical lens 90° and imaging Rayleigh scattering from ambient air, which represents the laser sheet profile. Pulse energies of approximately 400 mJ are used for the present measurements.

Scattering (from both gas-phase species and particles) is collected by two CCD cameras (PCO Sensicam; 19, 20) aligned normal to laser sheet. The first camera (19), denoted the *FRS camera*, is coupled to the I_2 filter cell as described above, to collect gas-phase Rayleigh–Brillouin scattering and ideally reject particle scattering. The second camera (20), denoted the *Mie camera*, simultaneously collects particle scattering. The *Mie camera* is outfitted with a series of neutral density (ND) filters (21) to attenuate the collected signals by more than four orders of magnitude. The ND filters serve two purposes: (1) to attenuate the particle scattering signal to acceptable levels such that the camera is not saturated (recall 400 mJ/pulse is used for the imaging) and (2) effectively reduce any Rayleigh–Brillouin scattering down to levels well below the noise floor of the camera such that the digitized signal output is a direct representation of the particle scattering only.

3 Results and discussion

3.1 I_2 Transmission scans

Measurements using the experimental configuration shown in Fig. 2a were first performed with a true single-frequency, narrow-linewidth (~5 kHz) CW Nd:YAG (JDS Uniphase NPRO M126N-1064-500) laser to compare with theoretical predictions and to estimate the lower bound of measurable transmission values for our current experimental system. The CW laser measurements were reported previously in [19] and are reproduced here for comparison with new pulsed laser results. As discussed in [19], the frequency-doubled CW laser was thermally tuned over the range of 18,786.6–18,788.1 cm^{-1}, which allows access to the strong R86(33,0)/R44(39,2) and R106(34,0) transitions near 18,787.3 cm^{-1}. The transmission profile for a 254-mm-long I_2 cell at temperature of 353 K and 1.05 Torr is shown in the left portion of Fig. 3 and denoted by the square symbols. As shown in Fig. 3 and discussed in [19],

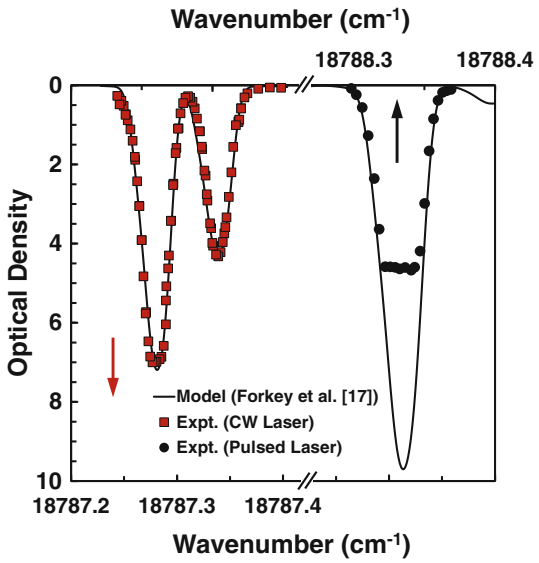

Fig. 3 Measured transmission profiles using a frequency-narrow CW laser (*red*, *square symbols*) and using an injection-seeded, Q-switched, pulsed laser (*black*, *circular symbols*). The CW laser scans were performed over the R86(33,0)/R44(39,2) and R106(34,0) transitions near 18,787.3 cm^{-1}. Cell conditions correspond to 353 K, 1.05 Torr, and 254-mm path length. The pulsed-laser scans were performed over the R56(32,0) transition near 18,788.3 cm^{-1}. Cell conditions correspond to 341 K, 1.05 Torr, and 254-mm path length. Also shown is the calculated transmission profile (*solid lines*) using the model reported by Forkey et al. [17]

the results using the frequency-doubled CW laser are in excellent agreement with the theoretical model predictions, consistent with the experimental results of Forkey et al. [17] who found the predicted minimum transmission and measured transmission with a CW laser agreed to within ±10 % for the six optically thick absorption lines in the frequency range of 18,787–18,789 cm^{-1}. The CW scan results show that the I_2 absorption spectra can be calculated accurately for the present measurement conditions and optical densities[1] of greater than seven can be measured in the present experimental configuration.

Figure 3 also shows updated transmission results using the pulsed laser for a 254-mm-long I_2 cell at a temperature of 341 K and pressure of 1.05 Torr. The pulsed laser was tuned over the frequency range of 18,787.8–18,789.6 cm^{-1}, which includes the strong R56(32,0) and P159(39,0)/P103(34,0)/P53(32,0) transitions of I_2 near 18,788.3 cm^{-1} as indicated by the "red" arrow in Fig. 1. For each frequency position, 250 transmission measurements were acquired. Similar to the CW laser-based transmission measurements, user-calibrated neutral density (ND) filters with optical densities ranging from 0.3 to 3.0 were placed as needed (depending on the

[1] The optical density is defined as $OD = -\log_{10}(T)$, where T is the transmission.

spectral overlap with the I_2 transitions) between the laser and the I_2 cell/photomultiplier tube combination as shown in Fig. 2a. Each ND filter transmitted a portion of the incident laser energy through the I_2 cell such that the laser light reaching the PMT was attenuated by a known amount. As the pulsed laser was tuned across an I_2 absorption line, ND filters were removed from the beam path to maintain a measurable PMT signal with high signal-to-background levels. In practice, removing a single ND filter of known OD was equivalent to rescaling the measured transmission by a factor of 10^{OD}. The effects of the continuous I_2 background (due to the $^1\Pi_{1u} \leftarrow X$ transition [17]) and optical cell transmission losses were accounted for by normalizing the measured resonant transmission values by the transmission values at a "non-resonant" position ($\sim$18,787.4 cm^{-1}). The typical standard deviation of the measurements was 3 % of the mean value. Consistent with previous results [e.g., 3, 10, 12, 15], the measured minimum transmission is much greater than calculated using the code of Forkey et al. [17], thus limiting the effectiveness of the I_2 filter. Specifically, for the current experimental conditions, the maximum measured optical density is 4.6 as compared to the maximum theoretical optical density of 9.7.

3.2 Estimation of laser spectral purity

The decrease in effectiveness of the I_2 filter is likely due to a decrease in laser spectral purity, where a small, but finite, broadband, non-seeded component exists within the laser output. In our previous work, we presented calculations showing the effects of decreasing laser spectral purity (SP) on realizable I_2 filter cell transmission [19] by modeling the laser output as a single-longitudinal mode superimposed onto a broadband pedestal. Briefly, summarizing the approach presented in [19], the seeded, single-mode output, $L_S(\nu)$, is modeled as a Gaussian distribution with a FWHM of 75 MHz, which was the measured linewidth of the frequency-doubled, pulsed laser. For cases of SP <1, the broadband, non-seeded component, $L_B(\nu)$, is modeled as a continuous Lorentzian distribution, which effectively describes the homogeneously-broadened distribution of Nd:YAG lasers [25]. The FWHM of the Lorentzian distribution is 42 GHz, which would be the result of frequency-doubling a 30-GHz (FWHM) bandwidth of the fundamental output at 1,064 nm as typically quoted by Nd:YAG laser manufacturers. The total modeled spectral distribution of the laser output is represented as $L_T(\nu) = L_S(\nu) + \alpha L_B(\nu)$, where α is free parameter proportional to the fraction of the total output energy contained within the broadband component. For the cases of SP <1, α can be increased such that the relative portion of the broadband Lorentzian distribution $L_B(\nu)$ is increased with respect to $L_T(\nu)$, which models an increasing fraction of energy being dispersed to additional longitudinal modes near the "seeded" longitudinal mode (i.e., a decrease in spectral purity). Consistent with previous definitions [26, 27], SP is defined as

$$SP = 1 - \frac{\int_{\nu_1}^{\nu_2} \alpha L_B(\nu) d\nu}{\int_{\nu_1}^{\nu_2} L_T(\nu) d\nu}. \quad (1)$$

where ν_1 and ν_2 are lower and upper frequency limits of integration, respectively, for a laser gain profile with a FWHM of 42 GHz.

To estimate the spectral purity of the current pulsed, Nd:YAG laser, the convolution of the modeled laser spectral distribution described by $L_T(\nu)$ and the I_2 absorption spectra over the R56(32,0) and P159(39,0)/P103(34,0)/P53(32,0) transitions of the $B(^3\Pi_{0+u}) \leftarrow X(^1\Sigma_g^+)$ electronic system of I_2 is performed for the experimental cell conditions corresponding to a pathlength of 254 mm, cell temperature of 341 K, and a cell pressure of 1.05 Torr. The free parameter, α, is varied, such that SP decreases from 1, until the calculated transmission curve (based on the convolution of $L_T(\nu)$ and the I_2 spectrum) matches the measured transmission spectra shown in Fig. 3. It is noted that this procedure accounts for both the fraction of the broadband component which is absorbed by the I_2 vapor (resonant and continuum absorption) and the fact that for the given cell conditions, even a laser with SP = 1 has finite transmission through the filter. The results of this process are shown in Fig. 4. The red, circular symbols are

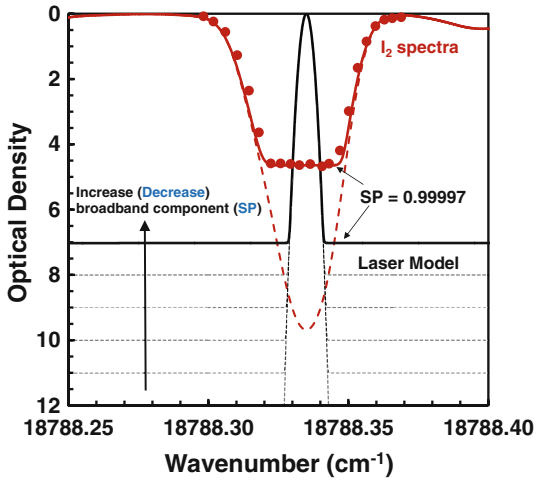

Fig. 4 Measured transmission profiles from Fig. 3 (*red*, *circular symbols*) matched to a calculated I_2 absorption spectrum for a laser spectral purity (SP) of 0.99997 (*solid*, *red line*). Also shown is the theoretical I_2 absorption profile (*red*, *dashed line*) for the experimental operating conditions. Example spectral distributions of the total laser output $L_T(\nu)$ with varying levels of a "non-seeded" broadband component are shown as the *solid gray lines*. The *solid black line* depicts the model of the laser output with SP = 0.99997

the experimental transmission data from Fig. 3. The dashed, red line is the theoretical model prediction using the code from Forkey et al. [17]. The solid, red line is the result of convolving the theoretical I_2 absorption spectrum (dashed, red line) with a laser output described by $L_T(v)$ with a spectral purity of 0.99997 as shown by the solid, black line. In this manner, the spectral purity of the current pulsed, frequency-doubled, Q-switched, Nd:YAG laser is estimated as 0.99997 (or 3×10^{-5} fractional broadband power). From these results, it is noted that a reduction is spectral purity by 30 parts-per-million leads to a decrease in realizable filter attenuation from an OD of 9.7–4.6 or more generally, the non-ideal laser output, in terms of spectral purity, of commercial injection-seeded, Q-switched, Nd:YAG lasers can limit the applicability of FRS significantly.

3.3 Fabry–Perot etalon design and specifications

To date, there are few reported approaches at increasing the spectral purity of the output of Q-switched, Nd:YAG lasers in the context of FRS imaging. One approach suggested the use of an intra-cavity etalon (placed within the laser cavity during pulse buildup) as a possible method to decrease energy contained in non-seeded longitudinal modes in the fundamental 1,064-nm output [15]. Using this methodology, reported suppression capabilities using the subsequent frequency-doubled output and an I_2 filter cell increased by approximately one order of magnitude. However, due to the highly fluctuating (thermal) conditions occurring within a laser cavity, intra-cavity etalons require precise temperature stabilization and frequency tuning.

This manuscript will demonstrate an alternative and more effective method to increase the spectral purity of the frequency-doubled, 532-nm output *directly* (as opposed to the fundamental 1,064-nm oscillator beam within the laser cavity) by reducing the energy contained within the broadband pedestal through spectral filtering with a tunable, Fabry–Perot etalon (FPE) placed in the optical beampath (see Fig. 2). A FPE is the simplest form of a Fabry–Perot Interferometer (FPI) and consists of two parallel highly reflecting surfaces used to form a multiple beam interference device. Strictly speaking, a FPE is one substrate which consists of two highly reflective surfaces, while a FPI consists to two parallel mirrors; however, convention is to denote an "etalon" (either solid or air-spaced) as a device with two parallel reflecting surfaces separated by a fixed distance, while an "interferometer" allows the distance between the reflecting surfaces to be varied. In this manuscript, we will consider the use of solid, fused silica FPEs and air-spaced FPEs, both with a fixed separation distance.

Detailed derivations of the amplitudes of transmitted waves through FPEs are given in several references [e.g., 28–30]. For the case of self-similar surface coatings; that is, the surface reflectivity (R_s) and surface transmission (T_s) are equivalent for both faces of the FPE, the transmitted intensity is written as

$$I_T = \frac{T_s^2}{(1-R_s)^2}\left[\frac{1}{1+F\sin^2(\varphi/2)}\right], \tag{2}$$

where F is the *coefficient of finesse* defined as $F = 4R_s/(1-R_s)^2$ and φ is the phase difference associated with the transmission of the electric field with each double pass within the FPE cavity. The phase difference φ *is* defined as

$$\varphi = 4\pi\mu d\cos\theta v, \tag{3}$$

where μ is the index of refraction, d is the cavity spacing, θ is the angle between the incident light rays and the surface, and v *is* the frequency of the incident light (in wavenumbers[2]). For the case of no surface absorption, $T_s = 1 - R_s$ and Eq. (2) reduces to

$$I_T = \left[\frac{1}{1+F\sin^2(\varphi/2)}\right], \tag{4}$$

which is the well-known Airy function [e.g., 31]. When the path length difference ($2\mu d\cos\theta$) of each transmitted beam is an integer multiple (n) of the incident frequency, then the phase difference φ is equal to $2\pi n$ and the FPE transmission is at a maximum. For φ values not equal to $2\pi n$, the transmitted intensity decreases by an amount proportional to the square of the finesse (F), which is defined as

$$F = \frac{\Delta v}{\delta v} \approx \frac{\pi\sqrt{F}}{2} = \frac{\pi R_s^{1/2}}{1-R_s}, \tag{5}$$

where δv is the full-width half-maximum value of the transmission profile and Δv is the frequency separation between adjacent transmission peaks known as the *free spectral range* (FSR). From Eqs. (4) and (5), it is obvious that FPEs with high finesse show sharp transmission peaks, narrower bandwidths, and lower minimum transmission.

In this study, we consider two FPE filters as described in Table 1: (1) a solid fused silica FPE housed in a temperature-controlled oven and (2) an air-spaced FPE consisting of two Zerodur (grade 0) spacers. The solid, fused silica FPE (VM-Tim Optomechanisch Werke, Germany) is 3.4 mm thick with surface reflectivity of 69 ± 1 % and a clear aperture of 20 mm. This leads to a theoretical (or *reflectivity*) finesse of 8.5, a coefficient of finesse of 29.7, a bandwidth (δv) of 3.5 GHz (0.12 cm^{-1}), and an FSR of 30 GHz (0.98 cm^{-1}). The VM solid, fused silica FPE is housed in an oven which is maintained at 318 K. The A5

[2] The conversion from spectroscopic frequency (units: cm^{-1}) to frequency (units: Hz) is $v(\text{Hz}) = \nu(cm^{-1})^* c$, where c is the speed of light with units cm/s.

Table 1 Fabry-perot etalon properties

Type	Spacer	d (mm)	Reflectivity	δν (GHz)[a]	Finesse	Est. Δν (GHz)/ °C
VM	Fused silica	3.4	69	3.5	8	5.54
A5	Air/Zerodur (0) spacers	5.0	88	1.2	25	0.55

[a] The bandwidth is given as the full width at half maximum (FWHM) of the transmission profile

air-spaced FPE (TecOptics, Merrick, NY) has a 20-mm-diameter clear aperture with 4.9957-mm-thick Zerodur (Grade 0) spacers. The surface reflectivity is 88 ± 2 % leading to a theoretical (or *reflectivity*) finesse of 24.6, a coefficient of finesse of 244, a bandwidth (δv) of 1.2 GHz (0.042 cm^{-1}), and an FSR of 30 GHz (0.98 cm^{-1}). However, it is well known that defects such as plate irregularities and non-ideal laser properties limit the theoretical performance of the FPE, where the effective finesse (F_e) is less than the theoretical "reflective" F and the transmission of the FPE will less than unity at the center frequency of the FPE. The effective finesse of the FPE can be estimated as

$$F_e = \left[\frac{1}{F^2} + \frac{1}{F_D^2} + \frac{1}{F_\theta^2} + \frac{1}{F_d^2} + \frac{1}{F_T^2}\right]^{-1/2}, \quad (6)$$

where F_D is the diffraction-limited finesse coefficient, which depends not only on the clear aperture, but the used portion of the aperture; F_θ is the beam divergence finesse coefficient, F_d is the defect finesse coefficient, which describes the effect plate spherical defects, spherical irregularities, and parallelism defects, and F_T is the tilt finesse coefficient describing a loss in finesse due to finite angle-tuning resolution or a mismatch between the angle, θ, prescribed by Eqs. (2) and (4) for peak transmission and the actual angle of the FPE with respect to the incident beam. In this work, the effective aperture (laser beam diameter) is 8 mm, the beam divergence is taken from the manufacturer's specifications as <0.1 mrad, and each FPE is mounted on a rotation stage with angular resolution of <0.7 mrad. Both FPEs have parallelism greater than $\lambda/100$ ($\lambda/200$ over the effective aperture) and sphericity of $\lambda/100$ over the clear aperture ($\lambda/500$ over the effective aperture). Combining all of these effects yields an estimate of F_e of 8 for the VM solid, fused silica FPE and 24 for the A5 air-spaced FPE. In addition, FPE defects and the non-ideal laser properties limit the transmission of the pulsed laser through the FPE. For the A5 air-spaced FPE, the calculated peak transmission is 95 %, and for the VM, fused silica FPE, the calculated peak transmission is somewhat higher at around 96–97 %. The measured transmission of the pulsed, 8-mm-diameter laser beam was approximately 90 and 95 % for the A5 and VM FPEs, respectively, which are consistent with the predicted values.

For a given frequency, the interference is a function of the optical pathlength and index of refraction between reflecting surfaces. Thus, by either changing the index of refraction or changing the effective distance between the reflecting surfaces of the FPE, a bandwidth of target frequencies can be preferentially selected to transmit through the FPE, while other frequencies are suppressed. For FPIs, the distance between the two mirrors can be adjusted through piezo-electric actuation or for both FPIs and FPEs, the effective distance between the reflecting surfaces can be changed by slightly adjusting the angle between the FPE and incident laser beam. The latter approach was taken in the current study. By careful selection of the initial fixed cavity spacing, angle tuning, and surface reflectivity (which determines the bandwidth), the FPE can act as a highly sensitive, ultra-narrowband filter. Figure 5 shows a calculation of the transmitted intensity for each FPE listed in Table 1 as a function of the tuning angle, θ. It is noted that the transmission is highly sensitive to tuning angle (or deviations from a given θ) and thus, in practice, care must be taken to achieve high transmission values. In addition, the optimal tuning angles are small and with increasing θ the effective bandwidth of the FPEs decrease. Figure 6 shows a calculation of the transmission of both the VM and A5 FPEs as a function of frequency with the tuning angles set such than the maximum transmission overlaps with the peak of the strong R56(32,0) I_2 absorption transition near 18,788.33 cm^{-1}. For this calculation, the tuning angle was 5.3 mrad or 0.3° for the A5 FPE and 9 mrad or 0.52° for

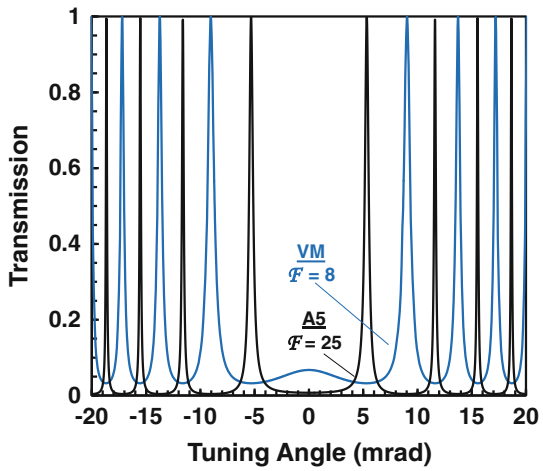

Fig. 5 Calculated transmitted intensity profiles as a function of tuning angle, θ, for the VM and A5 FPEs

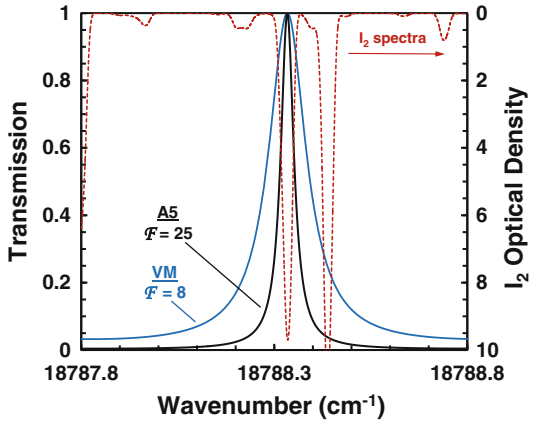

Fig. 6 Calculated transmitted intensity profiles for the VM and A5 FPEs as a function of spectral frequency. *Tuning angles* (5.3 mrad for A5 FPE and 9.0 mrad for VM FPE) are set such that the maximum transmission overlaps with the peak of the R56(32,0) I_2 absorption transition near 18,788.33 cm^{-1}

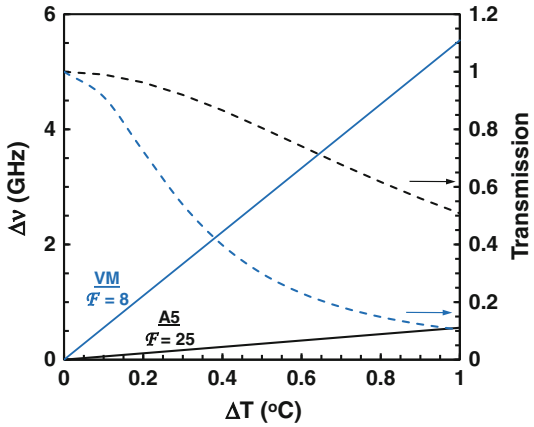

Fig. 7 Calculation of the sensitivity of the A5 and VM FPEs to small ambient temperature fluctuations in terms of the effective frequency shift ($\Delta\nu_s$) and corresponding loss in peak transmission. The results shown in "*blue*" and "*black*" are for the VM and A5 FPEs, respectively. The "*solid*" *lines* are the calculated temperature-induced frequency shift, and the "dashed" lines are the corresponding peak transmissions

the VM FPE. Figure 6 gives insight into the intent of the tunable FPE filtering methodology; that is, light from the laser in the frequency range within the bandpass of the FPE is transmitted (presumably the single longitudinal mode of the laser) and light in the frequency range outside of the bandpass of the FPE (presumably in the broadband pedestal of the laser output) will be suppressed heavily and will not transmit to the test section and contribute to the collected scattering. As an example, for the A5 FPE, laser light in the broadband pedestal can be suppressed by more than two orders of magnitude. Detailed calculations and experimental results showing the utility of the FPEs are presented in subsequent sections.

The design/specifications of the FPEs were tailored to the experiment to the extent possible. Recall that the transmission of the FPE is a strong function of the cavity spacing and the refractive index, both of which are sensitive to temperature fluctuations. Because the A5 FPE is an air-spaced FPE with low-thermal expansion Zerodur (0) spacers, small temperature fluctuations do not affect the transmission of the FPE significantly as shown in Fig. 7 and discussed below. In this manner, the bandwidth of the A5 FPE was chosen to match the bandwidth of the strong R56(32,0) I_2 absorption transition near 18,788.33 cm^{-1} as shown in Fig. 6. The rationale was that portions of the broadband pedestal within the A5 FPE bandwidth would transmit and contribute to unwanted particle scattering, but this scatter would still be subject to attenuation from the I_2 filter cell coupled to camera. However, it is noted that the transmission of the I_2 filter does vary with wavelength, and more specifically, the attenuation drops significantly away from the peak of the I_2 absorption line. In practice, a narrower bandwidth of the FPE could be chosen; for example, a bandwidth that is matched to the spectrally narrow laser bandwidth. However, this has to be considered in the context of the difficulty in maintaining alignment of an ultra-high finesse FPE with finite plate defects with a pulsed laser with finite beam diameter and divergence effects and the potential losses in transmission. Such a narrow margin in laser/FPE alignment may require a dynamic feedback/control system which is possible, but beyond the scope of this paper. In this manner, the bandwidth of the A5 FPE was chosen to be as spectrally narrow as possible, with the considerations of long-term alignment stability, targeting portions of the broadband pedestal whose scattering contribution would fall outside of the I_2 absorption transition.

The same design guidelines were not be applied to the VM solid, fused silica FPE. While solid, fused silica FPEs provide a low-cost alternative compared to air-spaced FPEs, they are much more sensitive to thermal fluctuations than air-spaced FPEs, which place a practical limit on the chosen finesse. To examine the effects of small temperature fluctuations on both FPEs, the effective frequency shift ($\Delta\nu_s$) and corresponding loss in peak transmission were calculated as a function of temperature fluctuations, ΔT as shown in Fig. 7. For each FPE, a fluctuation in temperature plays two roles: (1) It changes the refractive index of the cavity medium and (2) it changes the effective size of the cavity spacing, d, through thermal expansion effects.

For the air-spaced A5 FPE, the refractive index of air was calculated from 293 to 294 K in 0.1 K increments using the empirical formula of Birch and Downs [32]. Over the one-degree temperature range, the calculated refractive index of air changes by 0.9 parts-per-million. For the solid, fused silica FPE, the change in refractive index is

calculated as 1.28×10^{-5}/K [33]. The effective change in cavity distance of the FPEs can be estimated by considering the linear thermal expansion (α) of the Zerodur (0) spacers for the A5 FPE and the linear thermal expansion of the fused silica for the VM FPE. The linear thermal expansion coefficient for Zerodur (0) and fused silica are 2×10^{-8}/K [34] and 5.5×10^{-7}/K [35], respectively. In this manner, the new cavity distance $d'(\Delta T)$ as function of temperature is written as

$$d'(\Delta T) = d \pm 2\alpha \Delta T d. \quad (7)$$

Note that the cavity is assumed to decrease for a positive temperature change for the A5 FPE as the two Zerodur (0) spacers expand thermally, while for the solid, fused silica FPE, the cavity increases in size for a positive temperature change. Taking into account both refractive index and cavity spacing effects, the calculated frequency shift of the transmission profile of the FPEs is 0.55 GHz/K for the A5 air-spaced FPE and 5.5 GHz/K for the VM solid, fused silica FPE. Over a one-degree temperature fluctuation or long-term drift, the transmission of the A5 FPE would decrease to 55 %, while the transmission of the VM FPE would decrease to 10 %. In practice, observed room temperature fluctuations do not exceed 0.2 K, which only lowers the transmission of the A5 FPE by 4 %, which is deemed acceptable. For the same 0.2 K fluctuation, the transmission of the VM FPE would decrease by 30 %, which is not acceptable. In this manner, the VM fused silica FPE is placed within a temperature-controlled oven with specified temperature control to better than 0.1 K, which results in a maximum decrease in transmission of 9 %. From these results, it is clear that the bandwidth of the fused silica FPE was chosen as compromise between maximizing transmission and finesse. Further increases in finesse (or decreases in the bandwidth) may lead to unacceptable losses in transmission without additional experimental considerations such as active control.

3.4 Effects of spectral filtering pulsed 532-nm output with tunable Fabry–Perot etalons

To examine the potential benefits of the FPE-based spectral filtering, the FPE transmission profile (Fig. 6) is multiplied by the former model of the laser output, $L_T(v)$ (Fig. 4) to produce a "new" laser lineshape, $L_{T,\mathrm{FPE}}(v)$. This modeled laser profile is intended to represent the modified spectral distribution of the laser output after passing through either of the two tunable FPEs described above. Figure 8 shows the original model of the laser output (dotted black lines), a modified laser spectral distribution using the VM FPE (solid, blue line), and a modified laser spectral distribution using the A5 FPE (solid, black line). It is noted the single value of α, determined from the experiments shown in

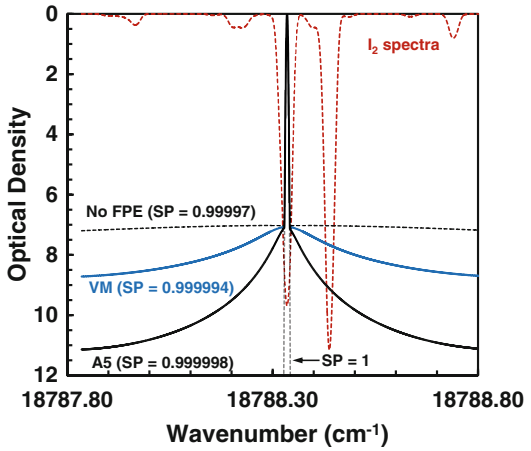

Fig. 8 Model of the original laser output, $L_T(\nu)$ (*dotted*, *black line*), a modified laser spectral distribution using the VM FPE (*solid*, *blue line*), and a modified laser spectral distribution using the A5 FPE (*solid*, *black line*). Also shown is the theoretical I_2 absorption profile (*red*, *dashed line*) for the experimental operating conditions

Figs. 3 and 4, is used for all three laser distributions. The differences between the modeled spectral distributions represent the effects of the FPE only. The calculated I_2 absorption spectrum also is shown for reference. Figure 8 clearly demonstrates the potential reduction in energy contained in the broadband pedestal of the laser output when using the FPEs. By comparing the total spectrally integrated energy contained within the broadband pedestal to that contained within the single longitudinal mode of the modified $L_{T,\mathrm{FPE}}$ profiles, an estimation of the effective increase in laser spectral purity is made as a result of implementing the VM and A5 FPEs. Using Eq. (1), the estimated spectral purity of laser output is increased from 0.99997 (3×10^{-5} fractional broadband power) to 0.999994 (6×10^{-6} fractional broadband power) and 0.999998 (or 2×10^{-6} fractional broadband power) when using the VM and A5 FPEs, respectively.

Figure 9 (solid lines) shows the calculated effects of the increased spectral purity in terms of effective optical density of the I_2 filter for our experimental conditions (pathlength of 254 mm, cell temperature of 341 K, and a cell pressure of 1.05 Torr). Similar to the procedure discussed above (and shown in Fig. 4) for the original modeled laser spectral distribution, $L_T(v)$, the modified model of the laser spectral distribution, $L_{T,\mathrm{FPE}}(v)$ is convolved with the I_2 absorption spectra over the $B(^3\Pi_{0+u}) \leftarrow X(^1\Sigma_g^+)$ electronic system of I_2. Shown in Fig. 9 are results over the R56 (32,0) transition near 18,788.33 cm^{-1}. The calculated result without the use of a FPE is shown with the solid, black line, while the calculated results using the VM and A5 FPEs are shown with the solid, blue, and red lines, respectively. As shown in Fig. 9, the predicted attenuation increases from an OD of 4.6 to 5.6 and 6.5 when using the

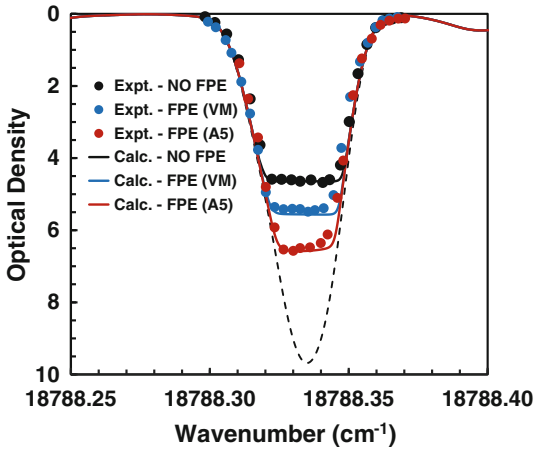

Fig. 9 The effects of the increased spectral purity (when using the FPEs) on the effective optical density of the I_2 filter. For the calculations, the spectral scans represent the convolution of the laser spectral distribution, $L_T(\nu)$ or $L_{T,FPE}(\nu)$ and the I_2 absorption spectra over the R56(32,0) and P159(39,0)/P103(34,0)/P53(32,0) transitions of the B ← X electronic system of I_2. No FPE = *solid*, *black line*; VM FPE *solid*, *blue line*; A5 FPE = *solid*, *red line*. Measured transmission profiles over the R56(32,0) transition near 18,788.3 cm^{-1} are shown as *solid symbols*. No FPE = *black symbols* (peak OD = 4.6); VM FPE = *blue symbols* (peak OD = 5.5); A5 FPE = *red symbols* (peak OD = 6.6). Conditions correspond to a cell temperature of 341 K, cell length of 254 mm, and cell pressure of 1.05 Torr

VM and AF FPEs, respectively. The latter case represents almost two additional orders of magnitude in light suppression in comparison of the case without the use of an FPE.

To experimentally verify the model calculations and to quantify the gains associated with the implementation of the FPE, experimental transmissions results across the R56(32,0) I_2 transition also are shown in Fig. 9 as solid symbols. The same experimental conditions and procedures are maintained as in the setup (shown in Fig. 2a) that produced the results shown in Fig. 3 (with the inclusion of the FPE in the optical beampath); that is, the FPE-filtered, pulsed laser output is directed through a series of user-calibrated ND filters with known ODs and through a 254-mm-long I_2 cell at a temperature of 341 K and pressure of 1.05 Torr. For each frequency position, 250 transmission measurements were acquired. As predicted by the model calculations, substantial increases in laser light attenuation are measured experimentally when using the FPEs. Furthermore, the experimental results for both the VM and A5 FPEs match the model calculations very well. For example, the peak measured attenuation is OD = 5.5 and 6.6 for the VM and A5 FPEs, respectively, as compared to the calculated values of OD = 5.6 and 6.5, respectively. The experimental results show two orders-of-magnitude increase in light suppression when using the A5 FPE to spectrally filter the pulsed, 532-nm output of an injection-seeded Nd:YAG laser.

3.5 Example FRS imaging

The utility of the FPE-based spectral filtering of the frequency-doubled Nd:YAG output for 2D FRS imaging in flows with particle scattering interference was demonstrated in turbulent, isothermal gas-phase jets, seeded with non-evaporating oil droplets, issuing into a co-flowing air stream. The experimental configuration for these measurements was described in Sect. 2 and shown in Fig. 2b. This configuration is intended as a "generic" experimental test bed to represent many environments with various levels of flowfield particulate (e.g., dilute spray environments, sooting flames, and simultaneous PIV/scalar measurements). Nonvolatile, liquid droplets are added to the gas-phase jets using a commercial aerosol generator (LaVision DS) commonly used for tracer particle generation in particle imaging velocimetry (PIV) studies. The aerosol generator produces a poly-disperse aerosol with diameters ranging from 0.2 to 1.0 μm, with a modal diameter of 0.25 μm and a median diameter of 0.5 μm. The concentration of the droplets in the jet fluid stream is controlled by the total gas flow rate through the aerosol generator, an internal pressure reducer within the aerosol generator, and the selective opening and closing of any of the four internal atomizing nozzles within the aerosol generator. The droplet-seeded jet fluid issues from a 7.75-mm tube into a 30 cm × 30 cm co-flowing air stream operating at 0.3 m/s. The co-flowing jet assembly is mounted on two high-precision translation stages that allow for translation in both axial and radial directions. In this manuscript, all reported images are centered at an axial position of $x/d = 10$, where d is the tube diameter.

Three turbulent jet conditions are considered: (a) a "dilute-seeded" N_2 jet operating at a Reynolds number (Re) of 2,100, (b) a "dilute-seeded" C_3H_8 jet operating at $Re = 5{,}100$, and (c) a "densely seeded" C_3H_8 jet operating at $Re = 11{,}200$. For the "dilute-seeded" cases, the particle volume fraction (F_{Vp}) is estimated as 5 parts-per-million (ppm) based on manufacturer specifications of droplet production rate (P), aerosol size distribution and operating jet fluid volumetric flow rate (Q). For both "dilute" cases, jet flow rates and aerosol generator settings are adjusted to produce the minimum droplet production rate, which is specified by the manufacturer as 1.4×10^{10} droplets/s. Using this production rate, the particle volume fraction, F_{Vp}, is calculated as $[1 + Q/(P^*V_d)]^{-1}$, where V_d is the weighted volume of a single spherical droplet based on the droplet diameter distribution. For the "densely seeded" C_3H_8 jet case, the particle volume fraction is estimated by using the ratio of the mean total particle scattering signal

per image from the "densely seeded" and "dilute-seeded" C_3H_8 jet cases. The ratio of the Mie-scattered light from the particles is proportional to the ratio of number of scattering droplets if all experimental parameters and droplet sizes are kept constant across the two experimental test cases. In this manner, F_{Vp} is estimated as greater than 60 ppm for the "densely seeded" C_3H_8 jet case.

Image processing of the FRS images first consists of the subtraction of darkfield and background signals. The darkfield is a fixed pattern offset that occurs with no light incident on the detector and is constant (in the absence of dark current and read noise) for all images acquired with the same exposure and read-out time. The "background" signal is that which arises from unwanted background light such as light scattering from optics and surfaces or the reflection of the particle scattering from optics, surfaces, etc. The typical procedure for accounting for the darkfield in many imaging experiments is to acquire a series of images with the shutter closed or lens covered, while the background is accounted for by acquiring images when the laser beam is present, but without the scattering medium [36]. However, the observed "background" in the presence of intense laser-based particle scattering may be different from the background obtained without the presence of particles. To account for the background signal in the presence of the seeded droplets, the field-of-view of the camera was adjusted such that the two-dimensional laser sheet used for the planar FRS imaging only occupied approximately one-fifth of the height of the CCD sensor. As described in Sect. 2, the laser sheet was formed by passing the laser beam through a single $f = 500$-mm, plano-convex cylindrical lens resulting in a laser sheet height of 10 mm. For the current measurements, the optical magnification is 0.13, which yields an imaged area of 65 mm × 52 mm, which after 2 × 2 hardware binning yields approximately 100 μm × 100 μm per pixel on the CCD sensors. In this manner, approximately 42 mm (or 840 rows of "inactive" pixels) of the CCD sensor lie above and below the "active" pixels (as defined by the laser sheet height) detecting scattered light. For the "dilute" cases, the combination darkfield/background signals, defined by the average signal of the "inactive" pixels, was equivalent to those obtained in cases with no particles present and with the lens cap on, indicating that the only signal offset was the fixed pattern darkfield, inherent to the camera itself. This is not completely surprising as the I_2 filter provides 4.5–6.5 (depending on whether the FPE is used) orders of magnitude of background light suppression. Thus, an average signal from a region of "inactive" pixels was subtracted from the FRS images, representing the contribution from the darkfield signal.

For the "densely seeded" case, the detected background was small but not negligible as evident by observed differences in the collected signals in cases with and without droplets in the "inactive" pixel regions. To estimate the background signal induced by the presence of the droplets, the region of the sensor corresponding to the "active" pixels (i.e., the location of the laser sheet and Rayleigh scattering) was first cropped from each image. This cropped region was then filled in by interpolating between the two remaining "inactive" pixel regions. This newly formed image served as an estimation of the total darkfield and background contributions present on each FRS-camera image and was subsequently subtracted from each FRS image.

The second image processing step involved the correction for pulse-to-pulse laser energy fluctuation and non-uniformity of the laser sheet intensity distribution. The laser sheet intensity correction was determined directly from the individual FRS images by measuring the instantaneous intensity magnitude and spanwise spatial distributions in a region of the uniform co-flowing air stream (after darkfield + background subtraction). The final image processing procedure involved 3 × 3 median filtering to increase the signal-to-noise ratio of the images.

The first test case considered is the seeded-N_2 jet operating at $Re = 2{,}100$ with a particle loading of approximately 5 ppm. After the aforementioned image processing, each individual image was normalized by the average signal from a 40 × 40 pixel region in the co-flowing air stream. Therefore, a normalized signal (S/S_{AIR}) of unity denotes pure air, $S/S_{AIR} = 1.04$ denotes pure N_2, and values of S/S_{AIR} between 1.0 and 1.04 denote some level of molecular mixing between the N_2 jet fluid and the co-flowing air. Values of S/S_{AIR} greater than 1.04 are assumed to be the result of scattering from the seeded particles transmitting through the I_2 filter cell and onto the detector. Figure 10 shows the probability density function (pdf) of three sub-cases associated with the N_2 jet; that is, (1) the same $Re = 2{,}100$ N_2 jet with NO particle seeding, (2) the seeded-N_2 jet imaged without a FPE in the optical beampath, and (3) the seeded-N_2 jet imaged with the A5 FPE in the optical beampath. The pdf for all three sub-cases is determined with 3.5×10^6 data points from 200 images. The "unseeded" N_2 jet experiment (solid black line) provides a baseline case for comparison to the "seeded" jet cases in terms of particle scattering rejection. The two dashed lines in the figure represent the ideal bounds between pure N_2 and pure air. While there are deviations in the pdf from the ideal bounds, it is noted that the pdf displays S/S_{AIR} over four orders of magnitude. For the unseeded N_2 jet case, 99 % of the measured S/S_{AIR} values are bound between 0.88 and 1.10. Since there is no particle scattering in the "unseeded" jet, this level of deviation from the ideal bounds ($1.0 \leq S/S_{AIR} \leq 1.04$) represents the combined effects of noise and image processing on the resultant S/S_{AIR}.

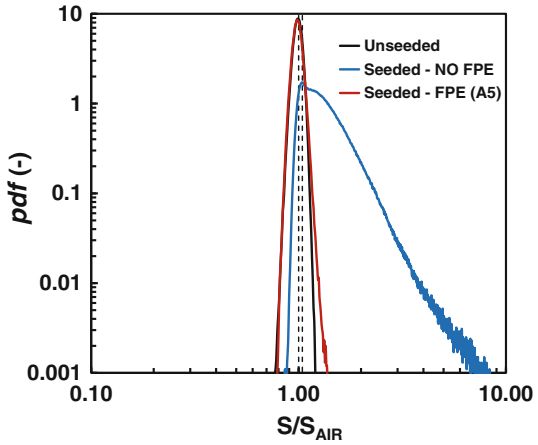

Fig. 10 Probability density function (pdf) results of the normalized signal, S/S_{AIR} in (*1*) an unseeded (no particles) N_2 jet (*solid black line*), (*2*) a seeded N_2 jet ($F_{Vp} \sim 5$ ppm) without the use of an FPE (*solid*, *blue line*), and (*3*) a seeded N_2 jet ($F_{Vp} \sim 5$ ppm) with the use of the A5 FPE (*solid*, *red line*). For all cases, the Reynolds number was 2,100

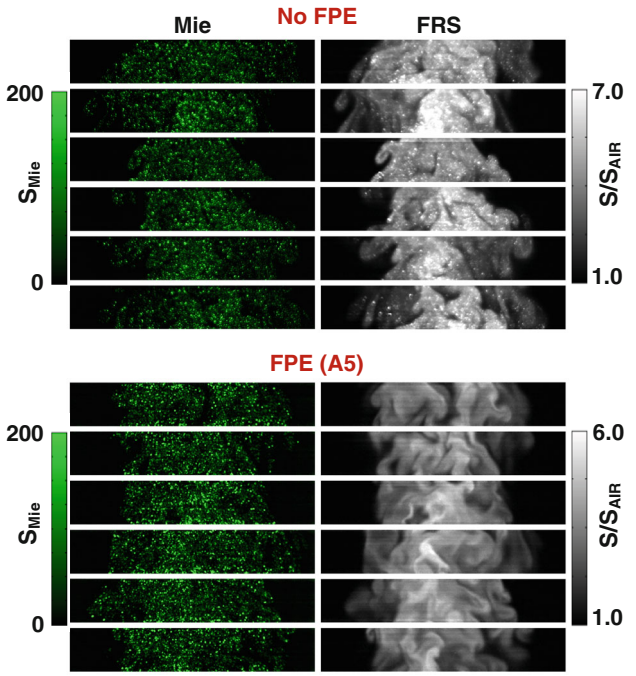

Fig. 11 Simultaneous particle scattering images (*left*) and FRS-camera images (*right*) in the "dilute-seeded" ($F_{Vp} \sim 5$ ppm) C_3H_8 jet operating at $Re = 5{,}100$. The images are centered at an axial position of $x/d = 10$. Each image corresponds to a field-of-view of 10 mm × 58 mm. *Top*—Images obtained *without* an FPE. *Bottom*—Images obtained *with* the A5 FPE. *Without* the FPE, particle scattering interference is observed on the FRS camera. When using the A5 FPE, no particle interference is noted

The pdf results of the FRS imaging of the seeded-N_2 jet without the use of an FPE are shown in Fig. 10 as the solid blue curve. The pdf noticeably deviates from the unseeded (baseline) case, with 81 % of the sample points yielding a value of $S/S_{AIR} > 1.10$. This indicates that a significant amount of particle scattering transmits through the I_2 filter cell. It is noted that the pdf is the result of particle scattering signals that have been suppressed by more than four and one-half orders of magnitude (through the I_2 filter); an attenuation factor that is more than an order of magnitude higher than previously reported within the literature [e.g., 10, 12, 15].

The pdf results of the FRS imaging of the same seeded-N_2 jet with the use of the A5 FPE as a spectral filter for the 532-nm output of the pulsed Nd:YAG laser are shown in Fig. 10 as the solid red curve. The pdf of S/S_{AIR} is essentially indistinguishable from that of the unseeded N_2 jet (baseline) case for more than three decades of values for $S/S_{AIR} < 1$ and more than two decades of values for $S/S_{AIR} > 1$. More specifically, more than 98 % of the sample points lie within the bounds of $0.88 \leq S/S_{AIR} \leq 1.10$, clearly demonstrating the increase in spectral purity of the Nd:YAG and the increased effectiveness of particle scattering suppression as compared to the case without the FPE.

Figure 11 shows two sets of image pairs from the "dilute-seeded", $Re = 5{,}100$ C_3H_8 jet issuing into a co-flowing stream of air. The top set of images was acquired without the use of an FPE as a spectral filter of the Nd:YAG output, and the bottom set of images was acquired with the A5 FPE in the optical beampath of the Nd:YAG laser to increase the spectral purity. For each image set, six simultaneously acquired image pairs are shown consisting of Mie (particle) scattering images and images from the FRS camera (ideally gas-phase signals) as discussed in Sect. 2 and shown in Fig. 2b. The Mie scattering images of the seeded particles are used to give the reader a sense of the particulate level in the flow and to identify potential locations of high particle scattering interference in the FRS images. Similar to the N_2 jets described above, each FRS image in the C_3H_8 jets was normalized by the average signal from a 40 × 40 pixel region in the co-flowing air stream.

Whereas N_2 and air have very similar Rayleigh scattering cross sections ($\sigma_{N2} \approx 1.04\sigma_{air}$), the scattering cross section of C_3H_8 is approximately 13 times higher than that of air. However, the amount of gas-phase signal that transmits through the I_2 filter and reaches the detector is determined by the convolution of the Rayleigh–Brillouin scattering lineshape, which is a function of the local thermodynamic conditions and gas composition, and the I_2 absorption transition lineshape, which is a function of the filter operating (thermodynamic) conditions [e.g., 3, 8, 10]. To determine the expected bounds of S/S_{AIR} for C_3H_8 issuing into air, the Rayleigh–Brillouin scattering lineshapes were calculated for both pure C_3H_8 and air using the

S6 code of Tenti et al. [37]. Subsequently, the calculated Rayleigh–Brillouin lineshapes were convolved with the calculated I_2 absorption spectra over the R56(32,0) and P159(39,0)/P103(34,0)/P53(32,0) transitions of the $B(^3\Pi_{0+u}) \leftarrow X(^1\Sigma_g^+)$ electronic system of I_2. For our experimental conditions (pathlength of 254 mm, cell temperature of 341 K, and a cell pressure of 1.05 Torr), approximately 14 and 26 % of the Rayleigh–Brillouin scattering signal is calculated to transmit through the I_2 filter for pure C_3H_8 and air, respectively. In this manner, the collected FRS signal is expected to be bound by $1.0 \leq S/S_{AIR} \leq 7.05$, where the latter value represents pure C_3H_8 jet fluid. Such signal levels yield a distinct contrast between pure jet fluid and pure air and allow observation of the gas-phase molecular mixing process between the jet fluid and co-flowing air stream. While pure C_3H_8 jet fluid may exist on any given instantaneous image, it should be noted that an axial position of $x/d = 10$ is beyond the jet potential core and the most probable FRS signal levels are the result between some level of mixing between C_3H_8 and air. Using the turbulent jet scaling relations of Tacina and Dahm [38], the mean centerline mixture fraction (ξ_{CL}), which describes the level of molecular mixing between two streams, is calculated as

$$\xi_{CL} = 5.4\left(\frac{x}{d}\right)^{-1}\left(\frac{\rho_{C3H8}}{\rho_{AIR}}\right)^{1/2} = Y_{C3H8,CL}, \quad (8)$$

where ρ_{C3H8} and ρ_{AIR} are the densities of propane and air, respectively, and $Y_{C3H8,CL}$ is the mean mass fraction of propane. Using Eq. (8), the mean centerline propane mass fraction at $x/d = 10$ is $Y_{C3H8} = 0.67$, which yields a mean centerline propane mole fraction, $X_{C3H8} = 0.57$ and a mean centerline $S/S_{AIR} = 4.4$.

Visual inspection of Fig. 11 leads to the clear observation of particle scattering "bleedthrough" on the FRS camera for the case of no FPE (top set of images). Since this jet has "dilute" seeding, individual particle scattering is observed as well as the accumulation of many particles yielding very high local signals. Figure 12 shows instantaneous radial profiles from each image in Fig. 11, extracted from an axial position of $x/d = 10$ (axial center of the image). In each image, the bounds of S/S_{AIR} corresponding to pure C_3H_8 and pure air are shown. For the case of "No FPE" (left column), several sharp, high-intensity peaks, which are much higher than the mean centerline value ($S/S_{AIR} = 4.4$) and even exceed that expected from pure propane ($S/S_{AIR} > 7$), are noted. These intensity signatures are undoubtedly due to particle scattering and act to mask the gas-phase information.

Conversely, the bottom set of image pairs in Fig. 11, which display FRS imaging results in the "dilute-seeded" C_3H_8 jet with the A5 FPE in the laser beampath, shows no visual evidence of particle scattering. The images highlight the gas-phase mixing between the propane jet and the surrounding co-flowing stream of air; that is, the gas-phase information appears to be captured without interference from the seeded particulate. Further evidence of this is shown in the right column of Fig. 12, which plots the radial profile at $x/d = 10$ from each of the images shown in Fig. 11. While the S/S_{AIR} profiles without the use of the FPE (left column) show ultra-sharp, high-intensity, signal spikes presumably from particle scattering, the S/S_{AIR} profiles acquired with the FPE spectrally filtered 532-nm output display realistic gradients expected within a turbulent mixing environment with the majority of the centerline S/S_{AIR} values near the expected mean centerline value of $S/S_{AIR} = 4.4$ and no S/S_{AIR} values exceeding that corresponding to pure C3H8 ($S/S_{AIR} = 7.05$).

Although the FRS methodology results in a reduction in collected signal due to scattering transmission losses through the I_2 filter, the FRS images acquired with the use of the A5 FPE shown in Fig. 11 (and Fig. 15 below) are of good quality. For example, after the 3×3 median filtering, the signal-to-noise ratio (SNR) of the FRS signal in pure air under the "dilute-seeded" conditions is 38, which is calculated as the mean value of S/S_{AIR} divided by the RMS fluctuation of S/S_{AIR} within a 40-pixel region of the co-flowing air stream. Under shot-noise-limited signal collection, the SNR for pure jet fluid can be estimated using a reformulated version of Eq. (8) from Ref. 36, $SNR = S_e/(S_e + N_{cam}^2)^{1/2}$, where S_e is the camera signal in units of electrons and N_{cam} is intrinsic noise of the camera, which includes the contributions from amplifier, thermal, dark-current shot, and quantization noise from the A–D converter. Since the SNR of the FRS measurements was derived in the co-flow (for a known $S_{e,AIR}$), N_{cam} is determined directly for the current camera and I_2 filter configuration. For pure C_3H_8 jet fluid, $S_e \approx 7^* S_{e,AIR}$ and the SNR is estimated as 100.

Figure 13 displays two sets of six simultaneous image pairs acquired in the "densely seeded" C_3H_8 jet ($F_{Vp} > 60$ ppm) operating at a Reynolds number of 11,200. Similar to Fig. 11, the top set of images was acquired without the use of an FPE as a spectral filter for the pulsed Nd:YAG output and the bottom set of images was acquired using the A5 FPE to increase the spectral purity of the Nd:YAG output. Again, the images in the left column are from the "Mie" camera, which collects particle scattering images and the images in the right column are from the "FRS" camera/I_2 filter combination intended to collect gas-phase Rayleigh–Brillouin scattering. First, it is noted that the particle fields (left column) are much denser with higher pixel signal intensity as compared to the images shown in Fig. 11 (the intensity scale being increased by a factor of ten as compared to Fig. 11), providing a more

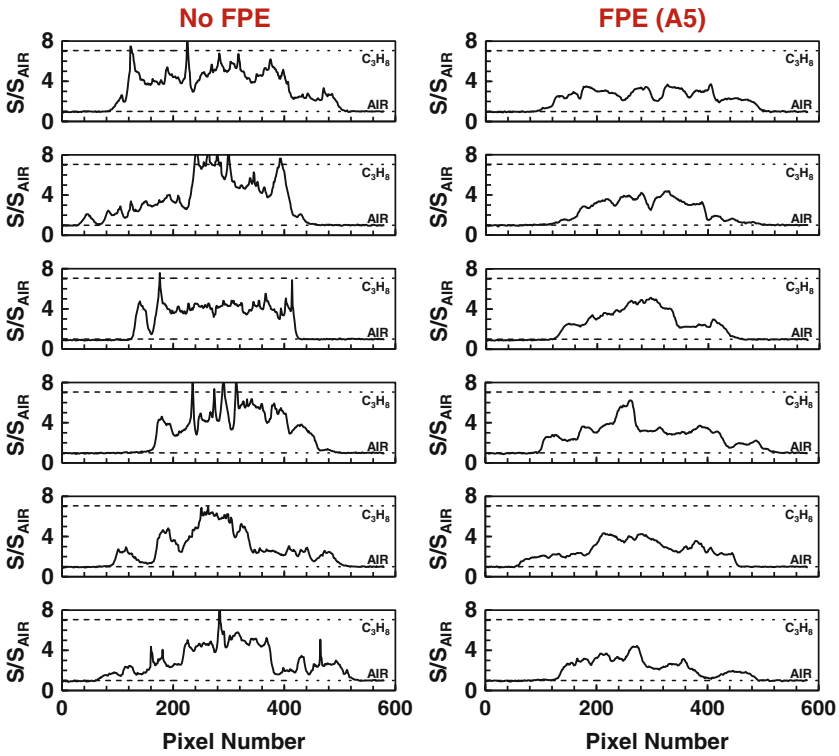

Fig. 12 Radial profiles of normalized signal, S/S_{AIR}, extracted from the instantaneous FRS-camera images shown in Fig. 13 at an axial position of $x/d = 10$. All figures are shown with "*dashed*" bounds corresponding to the expected normalized signal from air ($S/S_{AIR} = 1$) and pure C_3H_8 ($S/S_{AIR} = 7.05$). *Left column*—Profiles from images obtained *without* an FPE. *Right column*—Profiles from images obtained *with* the A5 FPE

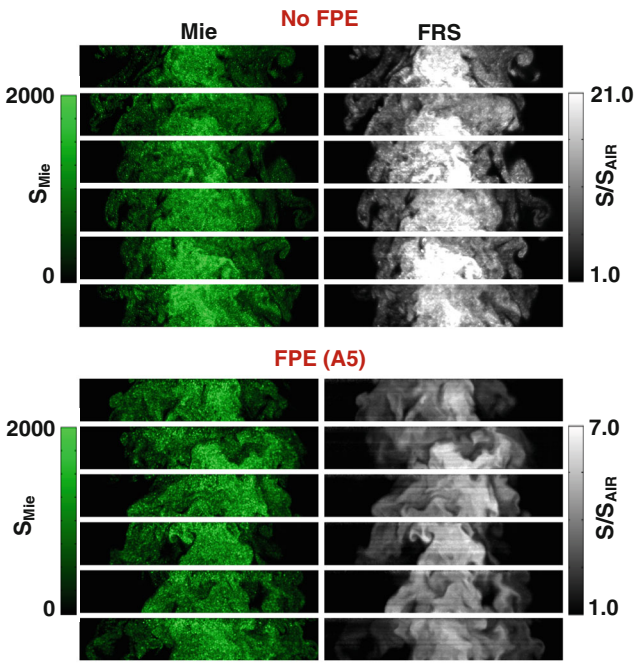

Fig. 13 Simultaneous particle scattering images (*left*) and FRS-camera images (*right*) in the "densely seeded" C_3H_8 jet ($F_{Vp} \sim 60$ ppm) operating at $Re = 11{,}200$. The images are centered at an axial position of $x/d = 10$. Each image corresponds to a field-of-view of 10 mm × 58 mm. *Top*—Images obtained *without* an FPE. *Bottom*—Images obtained *with* the A5 FPE. *Without* the FPE, significant particle scattering interference is observed on the FRS camera. When using the A5 FPE, no particle interference is noted

challenging environment for particle scattering suppression. Second, the intensity scales of the normalized FRS signals, S/S_{AIR}, are displayed from 1 to 21 for the case of "No FPE" and 1–7 when using the A5 FPE.

For the FRS-channel images in which no FPE was used, it is clear that the majority of the collected signal ($S/S_{AIR} > 21$) far exceeds what would be expected from the maximum gas-phase signals ($S/S_{AIR} = 7.05$). In this manner, we conclude that the signals are primarily from particle scattering and not gas-phase Rayleigh–Brillouin scattering, even with four to five orders of magnitude of particle scattering suppression afforded by the I_2 filter. This is further evident in the radial profiles extracted from the images as shown in Fig. 14. The left column shows single radial profiles taken from the axial center of the images shown in the top portion of Fig. 13. Three bounds are shown on the profiles corresponding to the expected normalized signal values from air ($S/S_{AIR} = 1$), pure C_3H_8 ($S/S_{AIR} = 7.05$), and saturation of the camera ($S/S_{AIR} = 24$). Signal saturation of the camera occurs at $S/S_{AIR} = 24$ due to the 12-bit nature of the camera (peak signal of 4,096 counts) in combination with the finite FRS signal from air and the contributions of the darkfield and background signals. Similar to the radial profiles shown in Fig. 12, ultra-sharp signal gradients characteristic of particle scattering are evident for the "No FPE" case with almost the full radial profile exceeding the maximum expected gas-

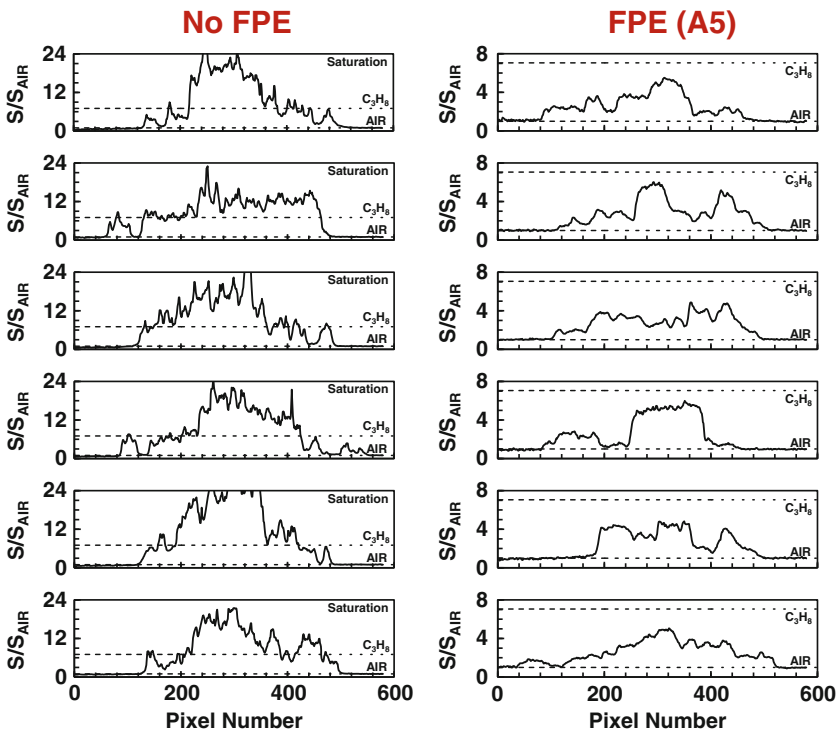

Fig. 14 Radial profiles of normalized signal, S/S_{AIR}, extracted from the instantaneous FRS-camera images shown in Fig. 15 at an axial position of $x/d = 10$. Figures are shown with "*dashed*" bounds corresponding to the expected normalized signal from air ($S/S_{AIR} = 1$), pure C_3H_8 ($S/S_{AIR} = 7.05$), and camera saturation ($S/S_{AIR} = 24$). *Left column*—Profiles from images obtained *without* an FPE. *Right column*—Profiles from images obtained *with* the A5 FPE

phase signals and a large number of instances saturating the camera. For this case (high particle seeding without the FPE), gas-phase Rayleigh–Brillouin scattering is not recoverable.

The bottom set of images in Fig. 13 shows the results obtained within the densely-seeded C_3H_8 jet when using the A5 FPE. Visually, the FRS images contain no evidence of particle scattering interference. The right column of Fig. 14 tentatively confirms this assertion as the extracted radial profiles show none of the ultra-sharp intensity spikes characteristic of particle scattering and the signals from the FRS camera are all bound between $1.0 \leq S/S_{AIR} \leq 7.05$. Figure 15 shows the mean S/S_{AIR} radial profile (plotted vs. the normalized radial position, r/d) at an axial position of $x/d = 10$ for both the "dilute-seeded" and "densely seeded" cases when using the A5 FPE to increase the spectral purity of the pulse laser source. The radial profile is extracted from the mean of 200 individual S/S_{AIR} images for each case. Also shown in Fig. 15 are signal bounds corresponding to pure air and the expected mean centerline signal ($S/S_{AIR} = 4.4$) based on turbulent scaling laws [38]. The measured mean centerline signal matches the expected mean centerline signal very well, indicating no influence of particle scattering. Thus, we conclude that when utilizing the A5 FPE to increase the spectral purity of the pulsed laser source, gas-phase Rayleigh–Brillouin signals are collected without interference from the flowfield particulate even for a level of particle seeding with volume fraction, $F_{Vp} > 60$ ppm.

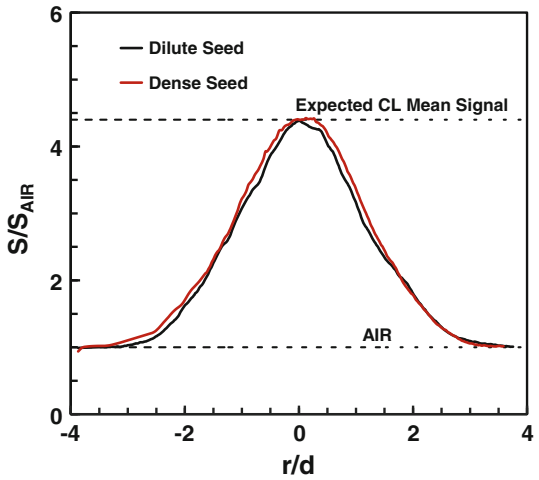

Fig. 15 Mean radial profiles of the normalized signal, S/S_{AIR}, at an axial position of $x/d = 10$ for both the "dilute-seeded" C3H8 jet (*solid*, *black line*) and the "densely seeded" C_3H_8 jet (*solid*, *red line*). Also shown are bounds (*dashed lines*) corresponding to the expected signal from air ($S/S_{AIR} = 1$) and the expected *centerline* signal ($S/S_{AIR} = 4.4$), obtained by considering turbulent jet mixing scaling laws [38]. Note the excellent agreement between the measured mean *centerline* signals and that expected from turbulent scaling laws

4 Conclusions

In this manuscript, tunable Fabry–Perot etalons (FPEs) were investigated as a method for spectrally filtering the visible, 532-nm output of injection-seeded, Q-switched, Nd:YAG lasers to increase the laser spectral purity and

increase the suppression of unwanted scattering for filtered Rayleigh scattering (FRS) measurements. In practice, the output of injection-seeded lasers is comprised of a single spectrally-narrow peak (the "seeded" longitudinal mode) superimposed onto a broadband pedestal of additional weak modes that form due to residual mode competition within the laser oscillator, thus reducing the spectral purity to less than unity. Previous work [e.g., 3, 7, 9, 10, 12, 15, 17, 19] has shown that the sub-unity spectral purity of the pulsed, Nd:YAG laser output severely limits the realizable attenuation of a molecular iodine-filtered Rayleigh scattering apparatus and thus limits FRS measurement sensitivity and the level of flowfield particulate in which FRS can be applied. The intent of utilizing an FPE in the optical beampath is to act as an ultra-narrowband spectral filter to transmit the desired spectrally-narrow peak of the laser while blocking a significant portion of the broadband pedestal of the frequency-doubled, 532-nm output.

The design and optimization of FPEs in the context of FRS imaging was discussed, and we demonstrated the performance of two particular FPE spectral filters: (1) a solid fused silica FPE (VM) housed in a temperature-controlled oven with a finesse of 8.5 and (2) an air-spaced FPE (A5) consisting of two Zerodur (grade 0) spacers with a finesse of 24. Transmission scans over the R56 (32,0) transition of I_2 near 18,788.3 cm^{-1} were performed using a 254-mm-long I_2 cell operating at a temperature of 341 K and pressure of 1.05 Torr. Measurements were reported with and without the use of the FPEs. For our current experimental conditions *without* the use of the FPE spectral filter, the maximum measured attenuation in terms of optical density was 4.6 as compared to the theoretical maximum optical density of 9.7. After implementing the FPE spectral filters, the peak measured attenuation was increased to optical densities of 5.5 and 6.6 for the fused silica and air-spaced FPEs, respectively, representing substantial increases in light attenuation. Based on the measured optical densities, we estimate that the laser spectral purity was increased by more than one order of magnitude from 0.99997 (3×10^{-5} fractional broadband power) to 0.999998 (2×10^{-6} fractional broadband power) when using the air-spaced, A5 FPE. Furthermore, calculations using a simple laser model [19] in conjunction with a theoretical FPE transmission profile yielded results that matched the experimentally determined transmission profiles to within 2 % for both FPEs.

The utility of the FPE-based spectral filtering of the pulsed Nd:YAG output for FRS imaging in flows with particle scattering interference was demonstrated in turbulent, isothermal gas-phase jets, seeded with varying levels of non-evaporating droplets. This configuration was intended as a "generic" experimental test bed to represent different environments with various levels of flowfield particulate. Statistical results in a "dilute-seeded" N_2 jet, with an estimated particle volume fraction (F_{Vp}) of 5 ppm, showed that the probability density function (pdf) of the measured FRS signals in the seeded jet *without* the use of an FPE noticeably deviated from a baseline, unseeded case (no particles). Greater than 80 % of the sample points yielded signal values much greater than the maximum signal bound defined by the "unseeded" case, indicating particle scattering interference. Conversely, the pdf results of the FRS imaging of the same seeded N_2 jet with the use of the A5 FPE as a spectral filter for the 532-nm output were indistinguishable from that of the baseline, unseeded jet for nearly three decades of values. These results indicated the increased effectiveness of particle scattering suppression as compared to the case without the FPE.

Additional sets of 2D imaging were performed in both a "dilute-seeded" C_3H_8 jet ($F_{Vp} \sim 5$ ppm) and a "densely-seeded" C_3H_8 jet ($F_{Vp} \sim 60$ ppm) issuing into an air co-flow. Visual inspection of both imaging cases shows clear particle "bleedthrough" on the FRS channel for the cases without the use of an FPE; and in the case of the densely seeded C_3H_8 jet (without an FPE), the particle scattering interference is sufficient to saturate the camera over the majority of the seeded domain, making gas-phase information unrecoverable. However, when utilizing the A5 FPE, no evidence of particle scattering interference is observed on the FRS channel, even for the densely seeded case. Mean radial profiles of the FRS signal for both the "dilute-seeded" and "densely-seeded" C_3H_8 jet cases yield results consistent with that expected from only gas-phase signals based on turbulent jet mixing scaling relations.

All of the aforementioned results indicate that the implementation of an FPE as a spectral filter for the frequency-doubled output of an injection-seeded, Nd:YAG laser is an effective method to increase the spectral purity by reducing the energy contained within the so-called broadband pedestal. The increases in laser spectral purity translate into increases in unwanted scattering attenuation and reduce or eliminate the interference from flowfield particulate in FRS imaging applications. For the current reported experimental conditions, gas-phase Rayleigh–Brillouin signals are collected without interference from the flowfield particulate for particle volume fractions of at least 60 ppm when using the A5 FPE.

Acknowledgments Support from the National Science Foundation (Dimitrios Papavassiliou, Program Manager) is greatly appreciated. The authors thank J. Forkey for supplying a version of the I_2 spectral code.

References

1. R. Miles, W. Lempert, Two-dimensional measurement of density, velocity, and temperature in turbulent high-speed air flows by UV Rayleigh scattering. Appl. Phys. B **51**, 1–7 (1990)

2. R.B. Miles, J.N. Forkey, W.R. Lempert, Filtered Rayleigh scattering measurements in supersonic/hypersonic facilities. AIAA Paper AIAA-92-3894, (1992)
3. J.N. Forkey, Development and Demonstration of Filtered Rayleigh Scattering—A Laser Based Flow Diagnostic for Planar Measurements of Velocity, Temperature, and Pressure, Ph.D. Dissertation (Princeton University, Princeton, 1996)
4. J.N. Forkey, N.D. Finkelstein, W.R. Lempert, R.B. Miles, Demonstration and characterization of filtered Rayleigh scattering for planar velocity measurements. AIAA J. **34**(3), 442–448 (1996)
5. R.B. Miles, W.R. Lempert, Quantitative flow visualization in unseeded flows. Annu. Rev. Fluid Mech. **29**, 285–326 (1997)
6. G.S. Elliott, M. Samimy, S.A. Arnette, A molecular filter based velocimetry technique for high speed flows. Exp. Fluids **18**, 107 (1994)
7. M. Boguszko, G.S. Elliott, On the use of filtered Rayleigh scattering for measurements in compressible flows and thermal fields. Exp. Fluids **38**, 33–49 (2005)
8. G.S. Elliot, T.J. Beutner, Molecular filter based planar Doppler velocimetry. Prog. Aerosp. Sci. **35**, 799–845 (1999)
9. G.S. Elliott, N. Glumac, C.D. Carter, Two-dimensional temperature field measurements using a molecular based technique. Combust. Sci. Technol. **125**, 351 (1997)
10. G.S. Elliott, N. Glumac, C.D. Carter, Molecular filtered Rayleigh scattering applied to combustion. Meas. Sci. Technol. **12**(4), 452–466 (2001)
11. D. Hofmann, A. Leipertz, Temperature field measurements in a sooting flame by filtered Rayleigh scattering (FRS). Proc. Combust. Inst. **26**, 945–950 (1996)
12. S.P. Kearney, S.J. Beresh, R.W. Schefer, T.W. Grasser, Filtered Rayleigh scattering diagnostic for multi-parameter thermal-fluids measurements: LDRD final report. Sandia Report, SAND2004-0158, 2004
13. D. Most, A. Leipertz, Simultaneous two-dimensional flow velocity and gas temperature measurements by use of a combined particle image velocimetry and filtered Rayleigh scattering technique. Appl. Opt. **40**(30), 5379–5387 (2001)
14. D. Most, F. Dinkelacker, A. Leipertz, Direct determination of the turbulent flux by simultaneous application of filtered Rayleigh scattering thermometry and particle imaging velocimetry. Proc. Combust. Inst. **29**, 2669 (2002)
15. R.G. Seasholtz, A.E. Buggele, Improvement in suppression of pulsed Nd:YAG laser light with iodine absorption cells for filtered Rayleigh scattering measurements. NASA Technical Memorandum 113177, 1997
16. J.N. Forkey, W.R. Lempert, R.B. Miles, Observation of a 100-MHz frequency variation across the output of a frequency-doubled injection-seeded unstable-resonator *Q*-switched Nd:YAG laser. Opt. Lett. **22**(4), 230–232 (1997)
17. J.N. Forkey, W.R. Lempert, R.B. Miles, Corrected and calibrated I2 absorption model at frequency-doubled Nd:YAG laser wavelengths. Appl. Opt. **36**(27), 6729–6738 (1997)
18. S.P. Kearney, R.W. Schefer, S.J. Beresh, T.W. Grasser, Temperature imaging in nonpremixed flames by joint filtered Rayleigh and Raman scattering. Appl. Opt. **44**(9), 1548–1558 (2005)
19. R.A. Patton, J.A. Sutton, Seed laser power effects on the spectral purity of Q-switched Nd:YAG lasers and the implications for filtered Rayleigh scattering measurements. Appl. Phys. B. **111**(3), 457–468 (2013)
20. A.P. Yalin, R.B. Miles, Ultraviolet filtered Rayleigh scattering temperature measurements with a mercury filter. Opt. Lett. **24**(9), 590–592 (1999)
21. A.P. Yalin, R.B. Miles, Temperature measurements by ultraviolet filtered Rayleigh scattering using a mercury filter. J. Thermophys. Heat Transf. **14**(2), 210–215 (2000)
22. A.P. Yalin, Y.Z. Ionikh, R.B. Miles, Gas temperature measurements in weakly ionized glow discharges with filtered Rayleigh scattering. Appl. Opt. **41**(18), 2753–3762 (2001)
23. J. Zetterberg, S. Li, M. Afzelius, M. Alden, Two-dimensional temperature measurements in flames using filtered Rayleigh scattering at 254 nm. Appl. Spectrosc. **62**(7), 778–783 (2008)
24. R.L. McKenzie, Measurement capabilities of planar doppler velocimetry using pulsed lasers. Appl. Opt. **35**(6), 948–964 (1996)
25. W. Koechner, *Solid-State Laser Engineering*, 6th edn. (Springer, Berlin, 2006)
26. N.P. Barnes, J.C. Barnes, Injection seeding I: theory. IEEE J. Quantum Electron. **29**(10), 2670–2683 (1993)
27. W. Lee, W.R. Lempert, Enhancement of spectral purity of injection-seeded titanium:sapphire laser by cavity locking and stimulated Brillouin scattering. Appl. Opt. **42**(21), 4320–4326 (2003)
28. E. Hecht, *Optics*, 2nd edn. (Addison-Wesley, Canada, 1987)
29. M. Born, E. Wolf, *Principles of Optics*, 6th edn. (Pergamon, Elmsford, 1980)
30. S.G. Lipson, H. Lipson, D.S. Tannhauser, *Optical Physics*, 3rd edn. (Cambridge University Press, London, 1995)
31. M. Abramowitz, I.A. Stegun, (eds.) "Airy Functions." Sec. 10.4 in "Handbook of Mathematical Functions with Formulas, Graphs, and Mathematical Tables", 9th printing. New York: Dover, pp. 446–452, 1972
32. K.P. Birch, M.J. Downs, Correction to the updated Edlén equation for the refractive index of air. Metrologia **31**, 315–316 (1994)
33. I.H. Malitson, Interspecimen comparison of the refractive index of fused silica. J. Opt. Soc. Am. **55**(10), 1205–1209 (1965)
34. A.G. Schott, Zerodur properties, www.us.schott.com. Retrieved 1 July 2013
35. Fused silica properties, www.us.schott.com. Retrieved 1 July 2013
36. N.T. Clemens, *"Flow Imaging", in Encyclopedia of Imaging Science and Technology* (Wiley, New York, 2002)
37. G. Tenti, C.D. Boley, R.C. Desai, Kinetic-model description of Rayleigh–Brillouin scattering from molecular gases. Can. J. Phys. **52**(4), 285–290 (1974)
38. K.M. Tacina, W.J.A. Dahm, Effects of heat release on turbulent shear flows. Part 1. A general equivalence principle for non-buoyant flows and its application to turbulent jet flames. J. Fluid Mech. **415**, 23–44 (2000)